RSC Advances

PAPER

Cite this: *RSC Adv.*, 2023, **13**, 770

Viable production of hydrogen and methane from polluted water using eco-friendly plasmonic Pd–TiO_2 nanocomposites†

Omar Mbrouk, *[a] M. Fawzy,[a] H. M. El-Shafey,[a] M. Saif,[b] M. S. A. Abdel Mottaleb [c] and H. Hafez[a]

Received 22nd November 2022
Accepted 12th December 2022

DOI: 10.1039/d2ra07442g

rsc.li/rsc-advances

Solar-to-fuel conversion is a novel clean energy approach that has gained the interest of many researchers. Solar-driven photocatalysts have become essential to providing valuable fuel gases such as methane and hydrogen. Solar energy has emerged as a renewable, abundant energy source that can efficiently drive photochemical reactions through plasmonic photocatalysis. As a capping agent, orange peel extract was used in this study in a microwave-assisted green method to incorporate titanium dioxide with distinct amounts (3, 5, and 7 wt%) from Pd-plasmonic nanoparticles (2–5 nm). The leading role for plasmonic nanoparticles made from Pd-metal is enhancing the photocatalyst's ability to capture visible light, improving its performance. X-Ray diffraction (XRD), X-ray photoelectron spectroscopy (XPS), transmission electron microscopy (TEM), Brunauer, Emmett, and Teller (BET) surface area analysis, and UV-vis DRS analyses have investigated the obtained plasmonic photocatalysts' crystallographic, morphological, and optical characteristics. The UV-vis absorption spectra demonstrated the visible light absorption capacity attributed to the localized surface plasmonic resonance (LSPR) behavior of the newly formed nanoplasmonic photocatalysts. The generated Pd–TiO_2 nanomaterials' photocatalytic activity has been examined and evaluated for combustible gas production, including the formation of CH_4 and H_2 from the photocatalytic degradation of Reactive Yellow 15 (RY) during a deoxygenated photoreaction in a homemade solar photobiogas reactor.

1 Introduction

In recent years, gases derived from fossil energy, such as CH_4 and H_2, have gained considerable attention as a "greener" renewable energy source.[1,2] As an alternative to nonrenewable energy sources, fuel-energy gases offer several advantages over conventional energy sources, including their reliability, cost-effectiveness, and environmental friendliness.[1,3] Providing fuel gases for ecological sustainability and energy challenges through solar-driven photocatalysts has become an essential solution.[4–6] Photocatalysis with plasmonics has emerged as a prominent and growing technology. The emerging technology enables the efficient use of sunlight as an abundant and renewable energy source to drive a variety of chemical reactions.[7] Based on TiO_2 and plasmonic nanoparticles (NPs), plasmonic photocatalysis is effective at separating charge carriers and tuning optical response to a broader range of wavelengths (visible and near-infrared).[8] Materials based on TiO_2 and plasmonic effects are in the lead of heterogeneous photocatalysis, which finds application in energy conversion systems, solar cells, wastewater treatment, and organic synthesis. The coupling of semiconductor photocatalysts with noble metal plasmonic nanoparticles (Au, Ag, Pd, and Pt)[9,10] has become a promising strategy to overcome the limitations of TiO_2. This is attributable to the characteristics of such plasmonic nanoparticles, which can effectively enhance the visible light absorption of the produced plasmonic photocatalysts through localized surface plasmonic resonance (LSPR) effects.[11,12] This prospective approach opens the door to several environmental applications, including green energy production, by enhancing the charge carrier separation and promoting the efficient light harvesting and absorption of the photocatalyst towards the visible region.[9,13]

Several synthetic methods have been employed to prepare plasmonic nano photocatalysts, including hydrothermal,[14] sol–gel,[15] microwave,[16] chemical and physical vapor deposition, gel combustion, and electrospinning.[17] Among these methods, microwave-assisted hydrothermal processes offer a clean, cost-

[a]*Nano-Photochemistry and Its Environmental Applications Laboratory, Environmental Studies, and Research Institute (ESRI), University of Sadat City (USC,), P. O. 32897, Sadat City, 23897 Menofia, Egypt. E-mail: omar.mbrouk@esri.usc.edu.eg*

[b]*Chemistry Department, Faculty of Education, Ain Shams University, Roxy, Cairo, Egypt*

[c]*Nano-Photochemistry, Solar Chemistry, and Computational Chemistry Laboratories, Department of Chemistry, Faculty of Science, Ain Shams University, Abbassia, 11566 Cairo, Egypt*

† Electronic supplementary information (ESI) available. See DOI: https://doi.org/10.1039/d2ra07442g

effective, energy-efficient, eco-friendly, rapid, and convenient method of heating, which results in higher yields in shorter reaction times.[16] Combining microwave synthesis with green chemistry is a new motivation that is considered an eco-friendly technique. Green synthesis methods based on plant extracts are among the best traditional physical or chemical processes. They do not require high-end equipment, do not produce hazardous by-products, and are of low cost and hence assessed as an environmentally friendly method.[18]

The present work uses an eco-friendly and fast green microwave-assisted hydrothermal method to synthesize Pd-plasmonic nanoparticles incorporated into TiO_2 nanoparticles to prepare smart dual functional plasmonic photocatalysts. This newly developed plasmonic photocatalyst has been applied as an efficient sunlight-driven nanomaterial for heterogeneous photocatalysis and photogeneration of valuable energy products such as CH_4 and H_2 as a novel approach from the anaerobic photocatalytic destruction of organic matter, using Reactive Yellow 15 (RY15) as a case of organic water pollution.

2 Experimental section

2.1 Materials

No further purification is required for the other chemicals, and all solutions are prepared with double-distilled water. Titanium(IV), isopropoxide (97%), palladium chloride ($PdCl_2$), and polyvinylpyrrolidone (PVP) are obtained from Fluka. The RY, C. I. Reactive Yellow 15 (RY15) dye, was manufactured by Dye Star Co., and has a chemical formula of $C_{20}H_{20}N_4Na_2O_{11}S_3$ and a molecular weight of 634.57 g mol^{-1}. Synthesis involves the use of orange peel extract as an environmentally friendly alternative in the process of preparing titanium dioxides.

2.2 Green synthesis of Pd–TiO_2 nanoparticles

Orange peel extract was prepared as described by Thi *et al.*, 2020,[19] with modification; it involves washing and drying fresh orange fruits before peeling them as thinly as possible. After dehydrating, the peel was ground and placed in an oven drier for 12 hours. Then, the solution of 1 g from the catalyst with 50 mL of double-distilled water with stirring. After macerating, the mix was set in a water bath for 1 h at 60 °C. The last step was to store the extract for later use in an argon environment.

Pd nanoparticles were produced by modifying the process given by Teranishi and M. Miyake.[20] In an improved method, the solution of (2.0 mM) H_2PdCl_4 was prepared by mixing 0.6 mmol of $PdCl_2$ and 0.2 M HCl. In order to control the size and morphology of palladium at the nanoscale, a 15 mL containing 2.0 mM H_2PdCl_4 aqueous solution with 35 mL from 40% ethanolic solution and 130 mg of PVP (1200 μmol) was refluxed for three hours under air. Using a 45 mL Parr microwave acid digestion jar, the solution mixture was irradiated for 3 min in a home microwave (running at 2450 MHz and 400 W). The final Pd product was dried at 80 °C in air.

Pd–TiO_2 plasmonic photocatalysts were prepared by adding proper quantities (3, 5, and 7 wt%) of Pd-metal to the hydrolyzed titanium isopropoxide solution. In a typical process, titanium(IV) isopropoxide (10 mL) was rapidly added to distilled water (100 mL), and a white precipitate was formed immediately. The residue was filtered using a glass frit and washed with 100 mL distilled water. The filter cake was added to a 160 mL mixture of 20 mL acetic acid and 0.1 M nitric acid in [1 : 2] orange extract : aqueous water solution under vigorous stirring at 80 °C until the slurry became a translucent blue-white liquid. The proportions (3, 5, and 7 wt%) of Pd-metal were added to the colloidal solution. The suspension was autoclaved in a vessel for 3 min in a household microwave oven[21,22] and the precipitate was then filtered, cleaned, and dried overnight at 50 °C to produce a dry powder, followed by calcination at 450 °C for removal of the residual organic matter.

2.3 Characterization

Using X-ray diffraction (XRD), we examined the surface morphology and scanning rate of Pd–TiO_2 plasmonic photocatalysts prepared with different Pd–TiO_2 combinations, with 30 mA, 40 kV, and 50 Hz scanning rates. To identify the morphology of nanomaterials prepared, a transmission electron microscope (TEM) JEM-2000EX (JEOL, Japan) with an acceleration voltage of 200 kV and a field emission gun (C-FEG) was utilized. The filament used in this TEM is a sharpened lanthanum hexaboride (LaB_6) crystal. A Jasco V-650 double-beam spectrophotometer was used to record UV-vis/DR spectra.

In this study, a BELSORP MINI X surface area and pore size analyzer was applied to determine the surface area and pore size distribution (adsorption–desorption of N_2 gas at 77 K). Under a nitrogen atmosphere, the samples were degassed at 150 °C for five hours before analysis. The X-ray photoelectron spectra (XPS) were retrieved using monochromatic Al K radiation and the Kratos Axis Ultra DLD apparatus (225 W, 15 mA, 15 kV), with a pass energy of 50 eV. The binding energy (BE) of adventitious carbon C ls (284.9 eV) was computed as a baseline.

2.4 Photoreactions

2.4.1 Photocatalytic degradation set-up. A UV-vis solar simulator (CHF-XM500, Trusttech Co., Ltd., China) has been utilized to investigate the photocatalytic activity of the produced Pd–TiO_2 nanomaterials compared to TiO_2 P25 nanoparticles. The photocatalytic experiment was carried out using an aqueous solution (100 mL from 5×10^{-5} M) of the RY15 as a model of organic dye pollutants *via* 0.1 g L^{-1} from the photocatalyst. After the absorption/desorption equilibrium of the solution on the catalyst surface, the slurry was subjected to 100 mW cm^{-2} simulated sunlight illumination. Aliquots were withdrawn and centrifuged at different time intervals to remove the catalyst. The absorbance of the clear filtrate was recorded on a Jasco-650 UV-vis spectrophotometer to follow the removal of the dye RY15 and evaluate the remaining dye concentration.

2.4.2 Fuel-gas generation set-up. All prepared samples were subjected to the biogas generation efficiency test through employing a prototype as described by Mbrouk *et al.*[23] The gas prototype A is a lab-scale UV reactor (ESI (S1)†), and the prototype concentrating solar reactor B is used under a nitrogen atmosphere for gas production. The photo-reactor A works with

UV energy. Ten (8 W UV-A) lamps make up reactor A, which is intended for anaerobic irradiation of the dye solution in the presence of a photocatalyst. An Aerocal gas detector is linked to this reactor to measure the quantity of CH_4 and H_2-generated gases. The irradiation of the average UV inside the photobiogas system ranges from 2.5 to 3.00 W cm^{-1}. Under the influence of stimulation by solar radiation, the gaseous products obtained from the reaction were measured. As optimization of environmentally friendly technology to reach the most efficient plasmonic materials for the ability to generate environmental energy products under direct sunlight. A compound parabolic concentrator and a borosilicate glass tube having a capacity of 500 mL make up reactor B (CPC).

3 Results

3.1 Morphological analysis

The TEM images of pure Pd plasmonic nanoparticles and Pd–TiO_2 nano photocatalysts compared with pure TiO_2 Degussa P25 nanoparticles are given in Fig. 1. The TEM image of Pd plasmonic nanoparticles (Fig. 1a) shows spherical nanoparticles with an average size of 2–5 nm that are well-dispersed with a uniform inter-particle separation. The HR-TEM image and EDX analysis of 5% Pd–TiO_2 are given in Fig. 1c and d, respectively; Pd–TiO_2 has been confirmed to form without altering the original morphology of TiO_2 during its formation. The HR-TEM images of P25 (Fig. 1b) show spherical nanoparticles with an average size of 10–15 nm.

3.2 XRD and XPS analyses

Fig. 2 displays the X-ray diffraction patterns of Pd plasmonic nanoparticles, P25, and Pd–TiO_2 nanoparticles. Three primary diffraction peaks at 40.1°, 46.6°, and 68.1° 2, which are attributed to the Pd (111), Pd (200), and Pd (220) phases, respectively, were seen in the XRD pattern of Pd-plasmonic nanoparticles. This matches the standard face-centered cubic (fcc) structure according to the JCPDS card no. 46-1043.[24] The XRD patterns of P25 and Pd–TiO_2 nanoparticles with different Pd loadings (3 wt% and 5 wt%) showed high crystallinity with the standard

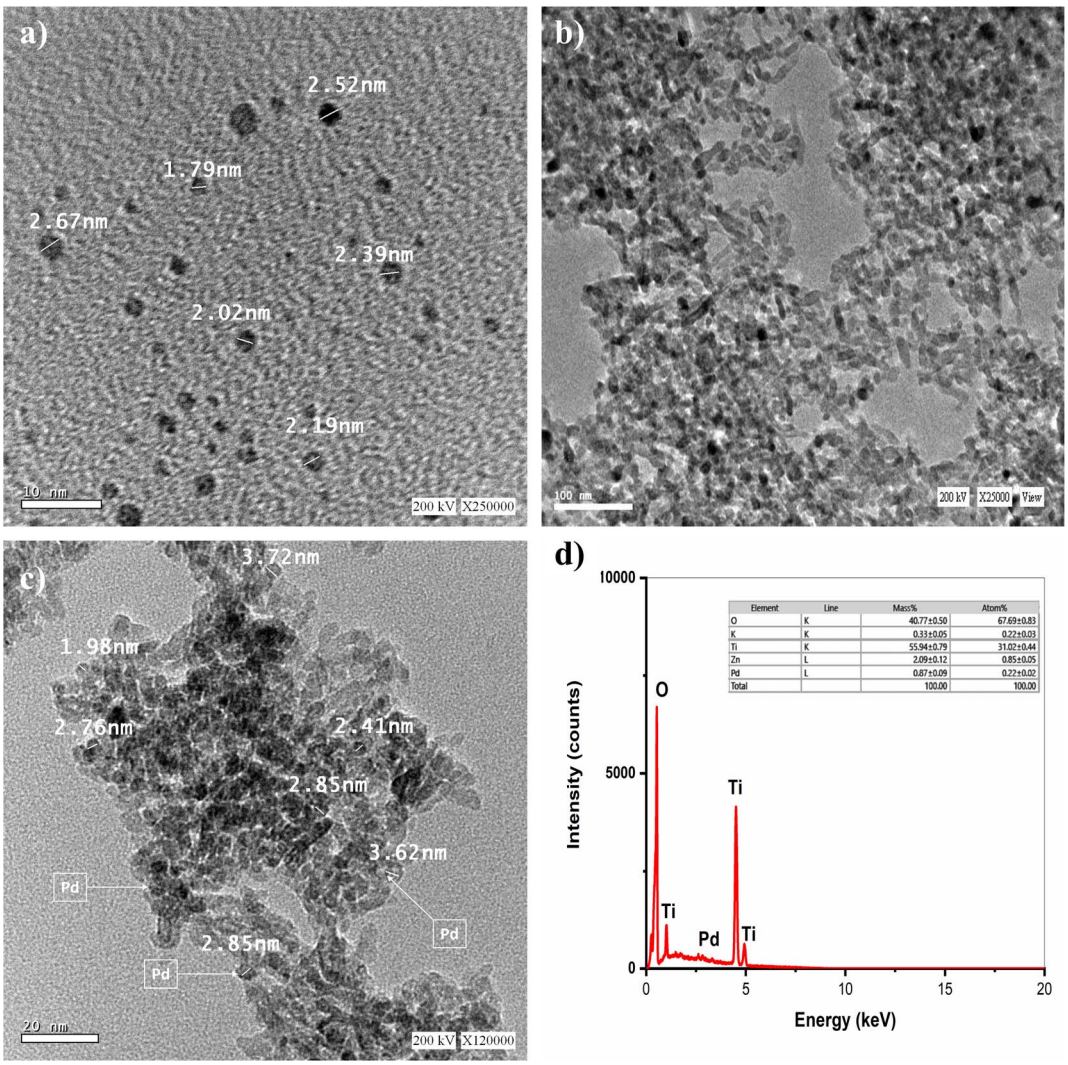

Fig. 1 HR-TEM images of: (a) Pd-metal; (b) TiO_2 P25; (c) 5% Pd–TiO_2; (d) EDX-analysis of 5% Pd–TiO_2.

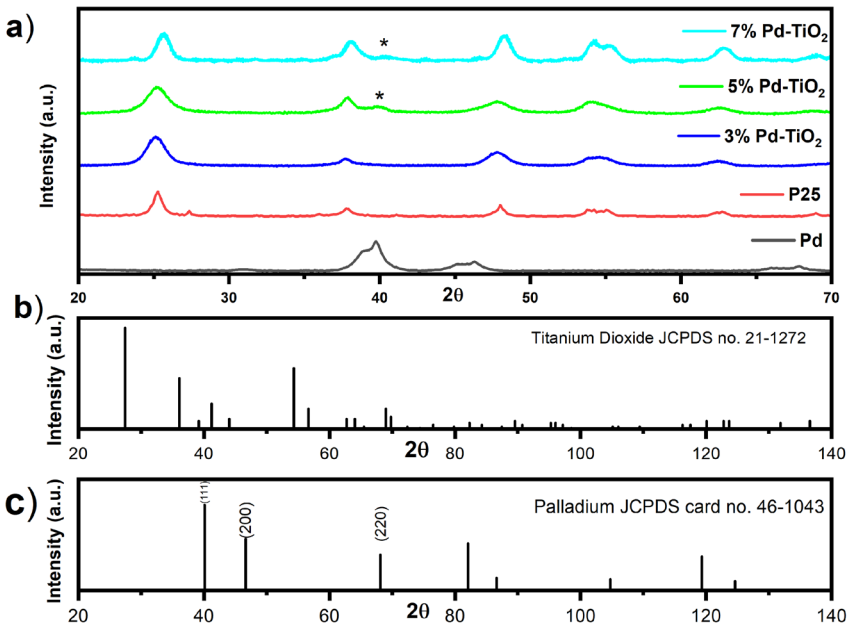

Fig. 2 (a) XRD patterns of Pd-metal, TiO_2 P25, 3% Pd–TiO_2, 5% Pd–TiO_2 and 7% Pd–TiO_2 nanoparticles, (b) pattern of JCPDS no. 21-1272 and (c) JCPDS card no. 46-1043 respectively.

peaks of pure anatase (JCPDS no. 21-1272), which is proven by the clear peaks obtained from all samples. Only one peak of Pd metal is seen at $2\theta = 40.1$ in both 5% and 7% wt Pd–TiO_2 samples, which refers to the face-centered cubic (FCC) Pd's (111) crystal plane spacing.[25] The other two peaks of the loaded Pd NPs were not observed in the 3% Pd–TiO_2 sample. This is because they overlap with the XRD diffraction peaks of anatase TiO_2 at $2\theta = 48$ and 68.1°. Fig. 2b and c shows the pattern of JCPDS no. 21-1272 and JCPDS card no. 46-1043, respectively.

The crystallite sizes of P25 and Pd-loaded TiO_2 nanomaterials were calculated by using Scherrer's formula eqn (1),

$$D = \frac{k\lambda}{\beta \cos \theta} \quad (1)$$

where D is the crystallite size (nm), k is a shape constant (in this case 0.9), λ is the wavelength of Cu K_α radiation (0.154 nm), θ is the diffraction angle (°), and β is the full width at half maximum. The data are given in Table 1. Doping with Pd-metal plasmonic nanoparticles is observed to reduce the average crystallite sizes of TiO_2 nanomaterials. To prevent aggregation and reduce the size of the TiO_2 NP, it was indicated that the metallic Pd is evenly distributed throughout the TiO_2 matrix and on the surface.[23]

XPS surface analysis was performed on TiO_2 P25, and 5% wt Pd loaded TiO_2 sample to investigate the Pd-metal content, Pd, Ti, and O (Fig. 3a–f). The leading characteristic peaks of Ti 2p, O 1s, and C 1s with their atomic ratios are shown in the XPS survey spectra (Fig. 3a and b) of P25 and 5% wt Pd–TiO_2 and are included in Table 2. Two distinct peaks for O 1s are present in the HR-XPS spectra of TiO_2 P25 and 5% Pd–TiO_2. They are attributed to the lattice oxygen (O_L) and the chemisorbed surface oxygen (O_S), which can either take the form of oxygen vacancies or hydroxyl oxygen,[27] respectively. Additionally, the binding energies of O_L and O_S in the P25 sample are located at BE = 529.69 eV and 531.59; for the Pd–TiO_2 selection, they are situated at BE = 530.03 eV and 531.77 eV (Fig. 3c and d).

The two HR-XPS peaks of TiO_2 are assigned to Ti(IV) titanium in the IV oxidation state of the diverse titania phases.[28] These peaks correspond to Ti $2p_{1/2}$ and Ti $2p_{3/2}$ spin-orbital splitting photoelectrons, which form at BE = 464.52 eV and 458.61 eV for P25 and BE = 464.36 eV and 458.77 for 5% Pd–TiO_2, respectively (Fig. 3e).

Table 1 The typical crystal sizes, band gap energies (E_g), $a_{s,BET}$, and photocatalytic performances of the produced Pd–TiO_2 nano photocatalysts

Sample	Average crystal size (nm)	E_g (eV)	E_{VB}	E_{CB}	$a_{s,BET}$ ($m^2\ g^{-1}$)	Total pore volume (p/p_0) $cm^3\ g^{-1}$	Average pore diameter (nm)	K_{app} (min^{-1})
TiO_2 (P25)	34.0[a]	3.08[a]	2.76	−0.32	56.191[a]	0.2537[a]	18.062[a]	0.036 ± 0.004
3% Pd–TiO_2	12.6	2.8	2.62	−0.18	82.971	0.2375	11.451	0.047 ± 0.005
5% Pd–TiO_2	11.2	2.4	2.42	0.02	96.451	0.2610	10.825	0.070 ± 0.005
7% Pd–TiO_2	9.4	2.13	2.29	0.16	104.85	0.2336	8.9133	0.097 ± 0.006

[a] Data from those estimated previously from ref. 26.

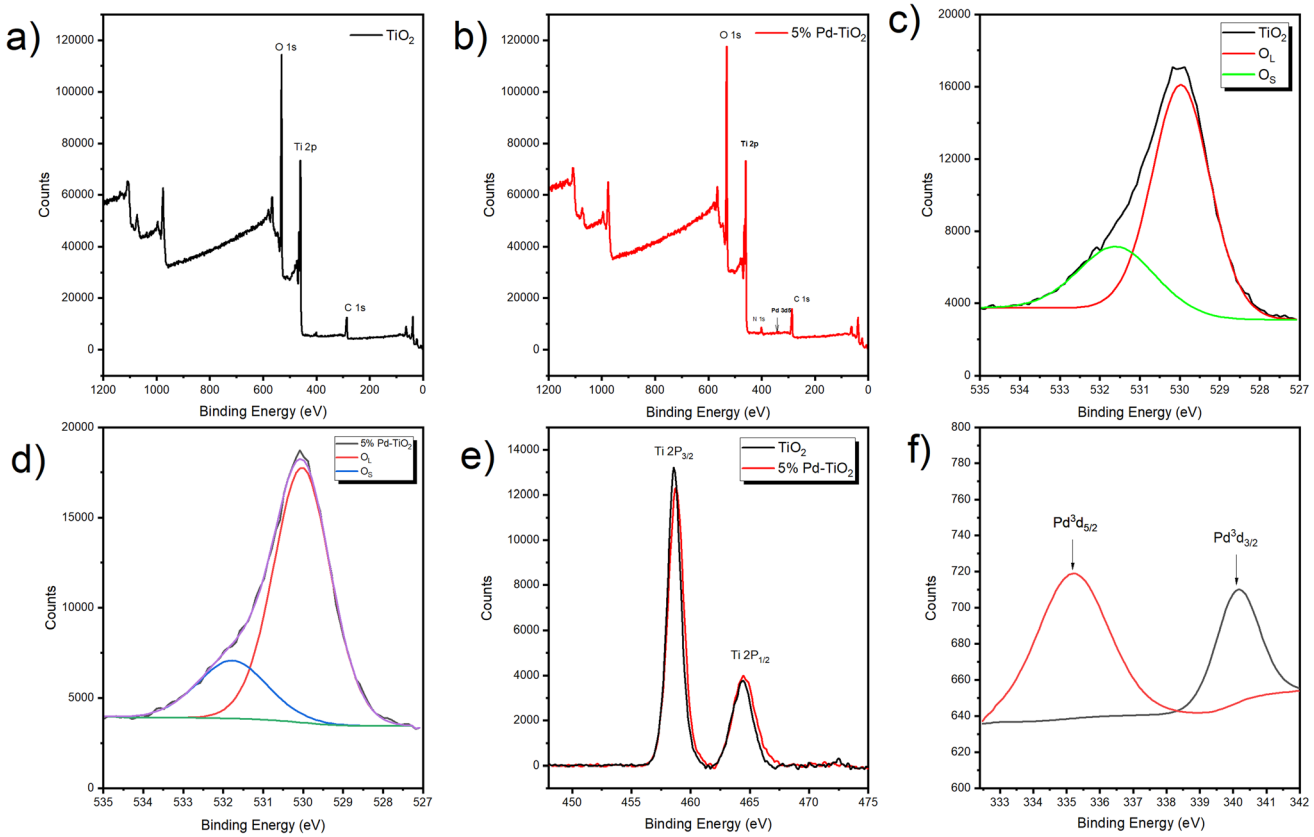

Fig. 3 XPS analysis of elements present in P25 and 5% Pd–TiO_2 (a and b) survey, (c and d) oxygen, (e) Ti, and (f) Pd.

Table 2 XPS data, binding energy values and atomic weight ratios of TiO_2 P25 and 5% Pd–TiO_2

	Binding energies (eV)						Atomic%			
	Ti 2p		O 1s		Pd 3d			O 1s		
Sample	$2p_{1/2}$	$2p_{3/2}$	O_S	O_L	$3d_{5/2}$	$3d_{3/2}$	Ti 2p	O_S	O_L	Pd 3d
TiO_2 (P25)	458.61	465.70	529.96	531.59	—	—	21.83	78.81 71.98	28.02	—
5% Pd–TiO_2	458.77	464.74	530.03	531.77	335.19	340.13	21.38	78.45 77.00	23.00	0.17

The Pd metal composition in the Pd–TiO_2 sample is further analyzed in Fig. 3f. The spectrum includes two spin–orbit doublets that involve a low-energy band peak (Pd $3d_{5/2}$ at BE = 335.19 eV) and a high-energy band peak (Pd $3d_{3/2}$ at BE = 340.13 eV). The spectrum of Pd $3d_{5/2}$ is given to zero-valent Pd-metal (Pd^0), which is well consistent with the literature value of the Pd $3d_{5/2}$ level binding energy Pd^0 (BE = 335.2).[29] Moreover, the Pd-HRXPS spectrum showed the presence of small PdO oxide peaks, revealing the presence of a mixture of Pd^0 and Pd^{2+} in the TiO_2 sample.[30] The few species from PdO can be attributed to the XPS being a surface test technology, and Pd NPs are only about 5 nm. Therefore, its surface is easily oxidized in the air.[31] This explains the slight increase in the atomic ratio of the lattice oxygen, O_L (from 72 to 77%), and the slight decrease in the chemisorbed oxygen, O_S (from 28 to 23%), in the Pd–TiO_2 sample.

3.3 Optical analysis

The optical absorbance spectra of the Pd-loaded TiO_2 nanomaterials were calculated using the UV-vis diffuse reflectance spectrophotometer, shown in Fig. 4a. Interestingly, the absorbance of Pd-doped TiO_2 in the visible region increases, which indicates that some trapping states have been formed with Pd metal plasmonic nanoparticles.[32] It has been demonstrated that a novel electronic state that lessens electron–hole recombination in the doped catalyst close to the CB has been produced. As a result, these nanoparticle photocatalysts will have enhanced photocatalytic activity. Moreover, the broadband with the max intensity at 470 nm in the visible region results from palladium metal surface plasmon absorption.[25]

The indirect band gap energies (E_g) are determined by plotting $F(\text{Alpha}*h\nu)^{1/2}$, where F(alpha) is the Kubelka–Munk

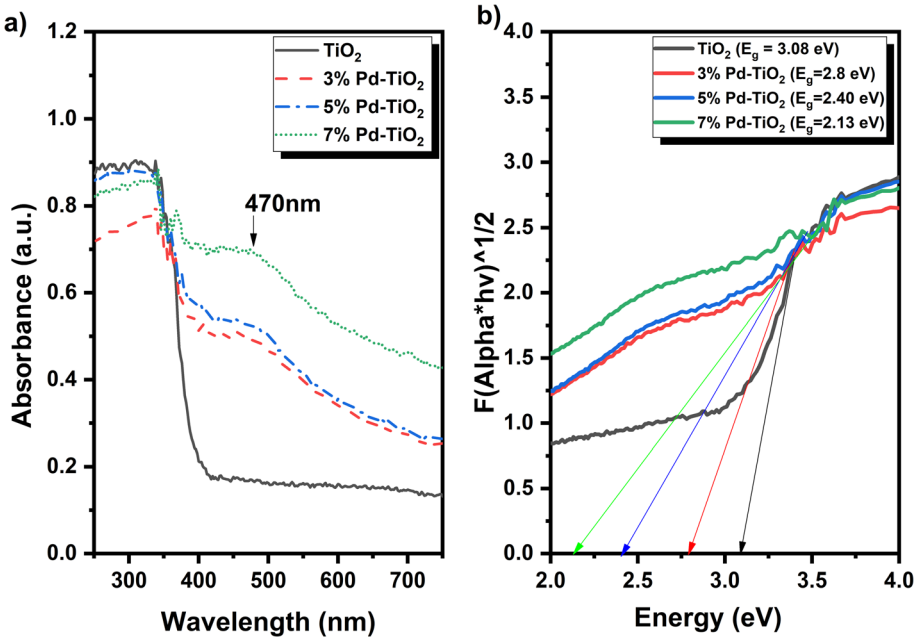

Fig. 4 (a) UV-vis absorption spectra; and (b) band gap energies of P25, 3 wt% Pd–TiO_2, 5 wt% Pd–TiO_2 and 7 wt% Pd–TiO_2 photocatalysts.

function,[33,34] as presented in Fig. 4b. The band gap energies of P25 and Pd-loaded TiO_2 NPs are calculated by extrapolating the linear part of the relative function curve to the energy axis. The E_g values are given in Table 1. The band gap energies of the TiO_2, 3% Pd–TiO_2, 5% Pd–TiO_2, and 7% Pd–TiO_2 samples were 3.08, 2.8, 2.4, and 2.13 eV, respectively. The decrease in band gap energies of TiO_2 by doping with Pd-metal plasmonic nanoparticles plays an essential role in the photocatalytic activity of the produced nano-plasmonic photocatalysts. The Butler and Ginley eqn (2) and (3) [35]

$$E_{VB} = \chi - E_e + 0.5E_g \quad (2)$$

$$E_{CB} = E_{VB} - E_g \quad (3)$$

where E_e is the energy of free electrons on the hydrogen scale and E_{VB} is the VB edge potential, where E_e is estimated to be 4.5 eV, while χ is the absolute electronegativity of the semiconductor. E_g is the bandgap energy of the individual photocatalyst. Besides, TiO_2 electronegativity is about 5.81 eV.[35]

3.4 BET surface area analysis

The nitrogen adsorption–desorption isotherms and the corresponding pore size distribution curves of the obtained nanoproducts are depicted in Fig. 5a–e, respectively. All samples have a type-IV isotherm with an H2 hysteresis loop, indicating that they are mesoporous nanostructured materials.[35] The variations in BET surface area, average pore size, and total pore volume after Pd loading based on the Barrett–Joyner–Halenda (BJH) method are summarized in Table 1. From the results in Table 1, it has been found that the specific surface area ($a_{s,BET}$) increases by increasing the amounts of Pd metal plasmons loaded in the TiO_2 matrix. This result is promising for enhancing the photocatalytic activity of the Pd–TiO_2.

3.5 Photocatalytic activity

As a model for organic dye pollutants, RY was applied to evaluate the photocatalytic activity of plasmonic photocatalysts synthesized under simulated sunlight illumination. The decay in the absorption spectrum of the aqueous dye solution in the presence of 0.1 g per L 5% Pd–TiO_2 photocatalyst is given in Fig. 6a.

The photocatalytic degradation rates of RY dye using P25 and Pd–TiO_2 nano photocatalysts under UV-vis irradiation confirmed pseudo-first-order kinetics described by eqn (4)

$$\mathrm{Ln}(A/A_o) = K_{app}t \quad (4)$$

where A_o is the absorbance at zero irradiation time, A is the absorbance at time t, and K_{app} (min^{-1}) is the apparent reaction rate constant. The $\ln(A/A_o)$ is plotted as a function of the irradiation time in Fig. 6b, and the results of the decomposition rate kinetic constant K_{app} values are given in Table 1. The results revealed that the photocatalytic activity of Pd–TiO_2 samples is much higher than that of P25. Moreover, it increases by increasing the amount of Pd-metal loaded. The photocatalytic activity of 7% Pd–TiO_2 is approximately three times that of P25. These findings reveal that the photocatalytic efficiency was improved by incorporating Pd-metal plasmonic nanoparticles into the TiO_2 nanomaterial. The increase in the photocatalytic activity of Pd–TiO_2 can be explained as Pd metal acts as an electron transfer pathway, decreasing the recombination of electron–hole pairs. This is in addition to the LSPR that enables Pd NPs to absorb light in the visible region, expanding the photocatalyst's transmittance in the visible area and enhancing

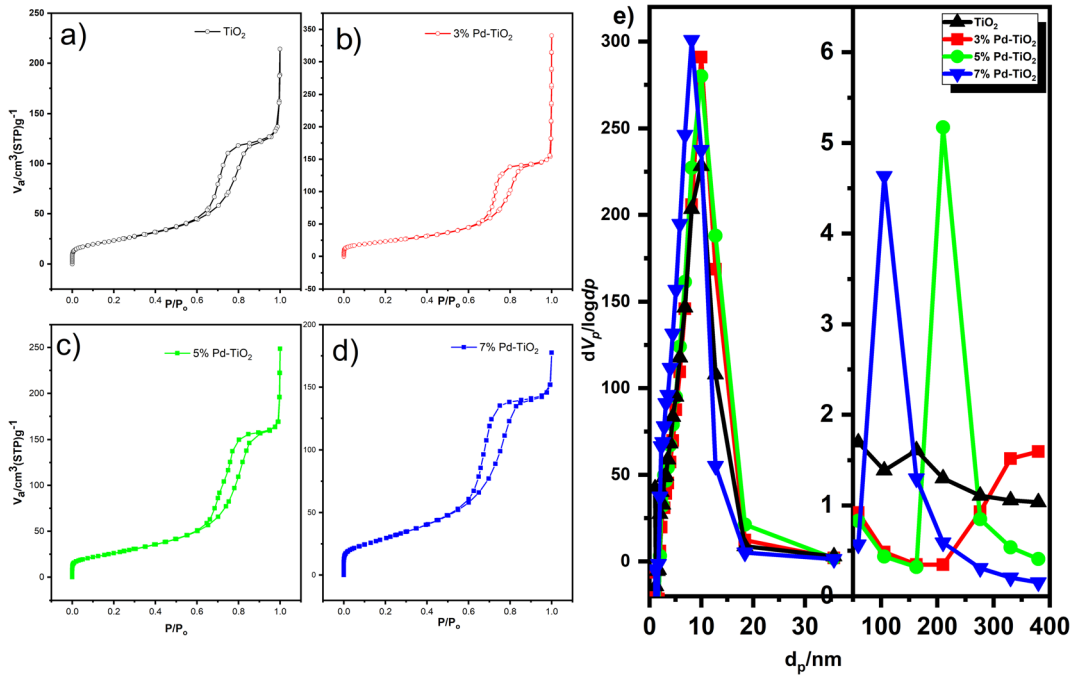

Fig. 5 Adsorption–desorption isotherms (a) TiO_2 (b) 3% Pd–TiO_2 (c) 5% Pd–TiO_2 (d) 7% Pd–TiO_2; and (e) pore size distribution of prepared TiO_2, 3 wt% Pd–TiO_2, 5 wt% Pd–TiO_2 and 7 wt% Pd–TiO_2 photocatalysts.

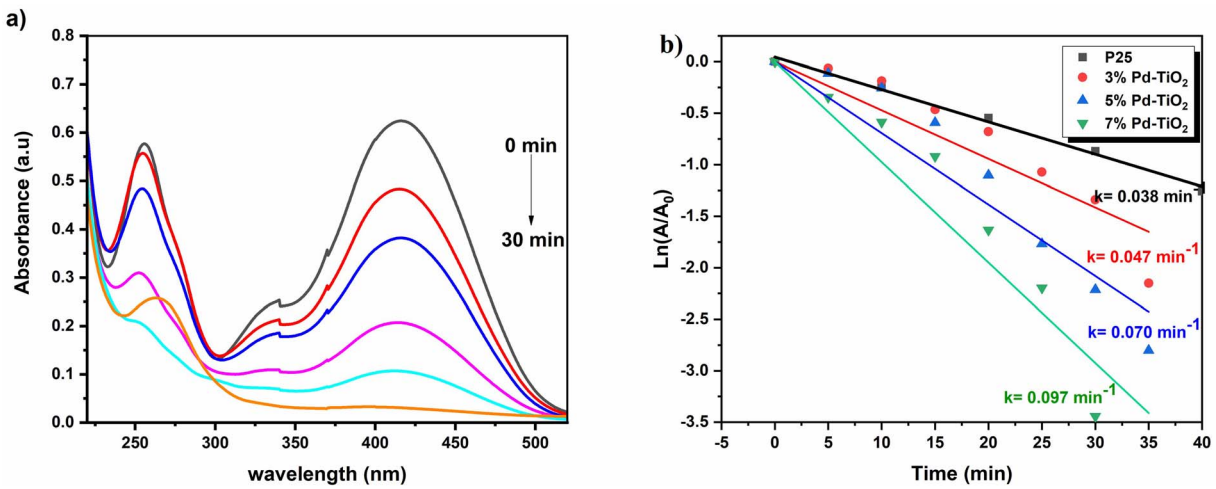

Fig. 6 (a) UV-vis absorption spectra of 5×10^{-5} M RY15 aqueous solution as a function of photoirradiation time with 0.1 g L^{-1} of 5 wt% Pd–TiO_2 photocatalyst, (b) the 1st order rate kinetics of the photocatalytic degradation reactions of RY15 using different plasmonic Pd–TiO_2 photocatalysts compared with P25 under UV-vis simulated sunlight illumination.

its photocatalytic activity toward the degradation of organic pollutants.[25,36]

3.6 Methane and hydrogen fuel gas generation

Firstly, the photo activities of the synthesized Pd–TiO_2 nanomaterials have been investigated in comparison with P25 under UV illumination in a designed homemade photoreactor (ESI (S1)†) under a nitrogen atmosphere. The total quantities of CH_4 and H_2 fuel gases created as degradation products after four hours of UV-irradiation are shown in ppm given in (Fig. 7a and b). Compared with the commercially available TiO_2 P25, the green synthesized Pd–TiO_2 photocatalysts possess higher yields for both CH_4 and H_2 fuel gases (Fig. 8). This can be ascribed to expanding the surface area of the TiO_2 matrix by adding Pd-metal nanoparticles.

From the practical point of view, the photocatalytic activity of the prepared Pd–TiO_2 plasmonic photocatalysts was evaluated on CH_4 and H_2 gas generation from the anaerobic photocatalytic decomposition of the RY organic dye pollutant under sunlight radiation in a pilot solar photoreactor. The amounts of

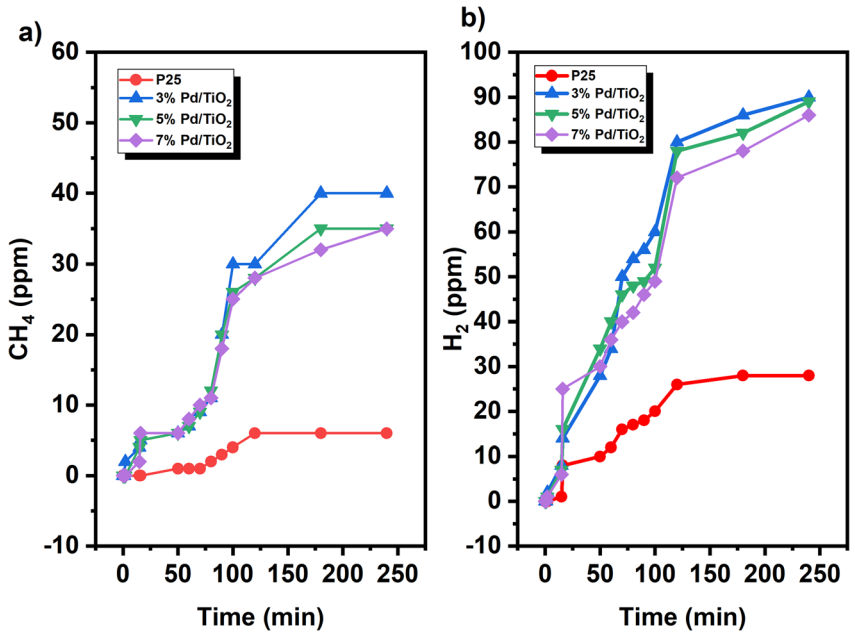

Fig. 7 Generation rate of methane and hydrogen gases in ppm as a function of time during the photocatalytic destruction of RY15 as a model of organic dye pollutant, under UV illumination in a homemade photoreactor using the different plasmonic Pd–TiO_2 photocatalysts compared with TiO_2 (Degussa P25).

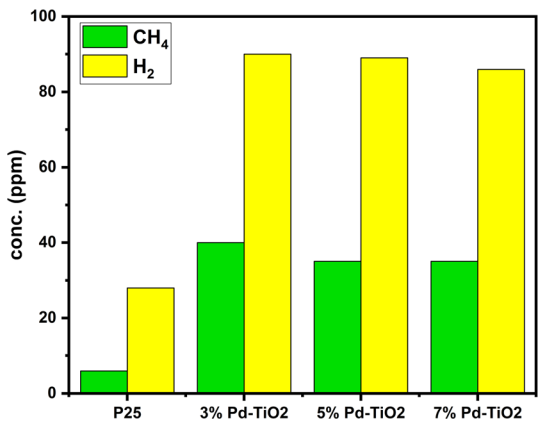

Fig. 8 Bar presentation for the generated amounts of CH_4 and H_2 gases in ppm after 4 h of illumination.

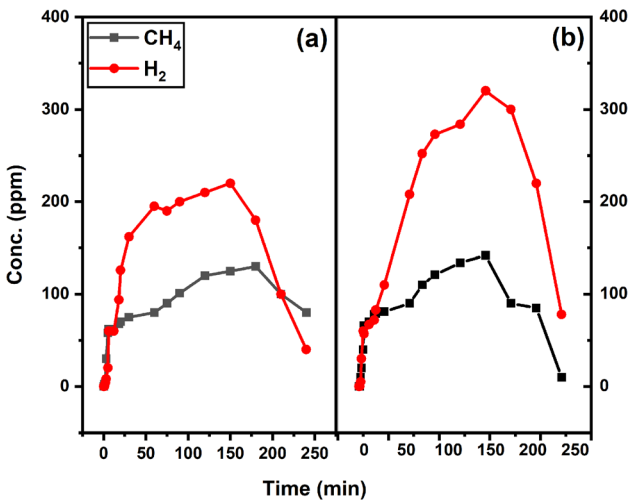

Fig. 9 Methane and hydrogen generation rates in ppm as a function of irradiation time produced from the photocatalytic destruction of RY15 dye pollutants using P25 and 5% Pd–TiO_2 photocatalysts.

CH_4 and H_2 gases in ppm generated after 3 h of sunlight illumination from the photocatalytic destruction of RY15 dye employing TiO_2 P25 and 5% Pd–TiO_2 photocatalysts are compared.

The results are presented in Fig. 9. Higher considerable amounts of CH_4 and H_2 gases are evolved. This is owing to plasmon resonances produced by visible light, increasing light absorption in the visible range and amplifying surface electron excitation. Based on these findings, it is shown that Pd-metal plasmons have a noteworthy influence on TiO_2 photocatalyst absorption in the visible spectrum, resulting in enhanced photocatalytic performance.

The conductivity of palladium remains excellent when its dimensions are in the NP range. The metal surface traps electrons and holes, which makes it an excellent material for transporting charge carriers. This is valuable for applications that require quick charge carrier transmission to obtain the required outcomes. The SPR effect is achieved through the interaction of palladium and titanium dioxide with incident light. As incident light excites the collective electrons of this Pd, surface plasmons are created as the electron density oscillates rapidly throughout the palladium nanoparticles.[37] Then the frequency of the electron cloud will resonate with the frequency of the incident light, causing an intense, uniform, local electromagnetic field to form on the NP surfaces.[38] Through

plasmonic coupling, the electromagnetic field may be amplified. When the fields of adjoining NPs apply pressures on one another, the near-field dipolar coupling phenomenon occurs. This excitation happens when the polarisation is perpendicular to the connecting axis in the transverse mode and parallel in the longitudinal mode.

The electrons of all plasmonic nanoparticles oscillate in the same phase intrinsically, and the ensuing charge distribution of surrounding plasmonic nanoparticles repels the dipoles in the transverse phase. This is owing to an increase in their restoring force, whereas the dipoles in the longitudinal phase are attracted due to a drop in their restoring force (Fig. 10), and the electromagnetic field distribution may widen from a surface vicinity of 5 nm for a single Pd NP to the whole region between neighboring NPs (30 nm).[39] As a result, the former red-shift (longitudinal mode) or a blue-shift (transverse mode) of the resonant wavelength the absorption spectra expand, causing two absorption peaks and a decrease in radiative scattering.

The following equations depict a hypothesised mechanism for the anaerobic photo-activated process over Pd–TiO_2 photocatalysts.[40,41] Fig. 10 is a schematic diagram drawn to show the equations in a graphical way. Direct illumination of Pd–TiO_2 photocatalysts results in the ejection of a valence band electron into the CB, resulting in the creation of the charge carriers e^- and h^+ (eqn (5)) on the TiO_2 photocatalyst surface.[42]

According to eqn (6), Pd metal will scavenge the conduction band electron (e^-). Consequently, the reactive oxidizing species ·OH generated from the interaction between photogenerated h^+ and H_2O molecules (eqn (7)). The final reaction equation reveals the production of CO, CO_2, and photodegradation by-products as a result of oxidation of dye solution by the active oxidiser ·OH or h^+ (eqn (8)).

$$TiO_2 + h\nu \rightarrow TiO_2\,(e^- + h^+) \quad (5)$$

$$TiO_2\,(e^-) + Pd \rightarrow TiO_2 + Pd\,(e^-) \quad (6)$$

$$H_2O + h^+\,(TiO_2) \rightarrow H^+ + OH^{\cdot} \quad (7)$$

$$\text{Dye} + \cdot OH \text{ or } h^+ \rightarrow \text{other degradation products} + CO + CO_2 \quad (8)$$

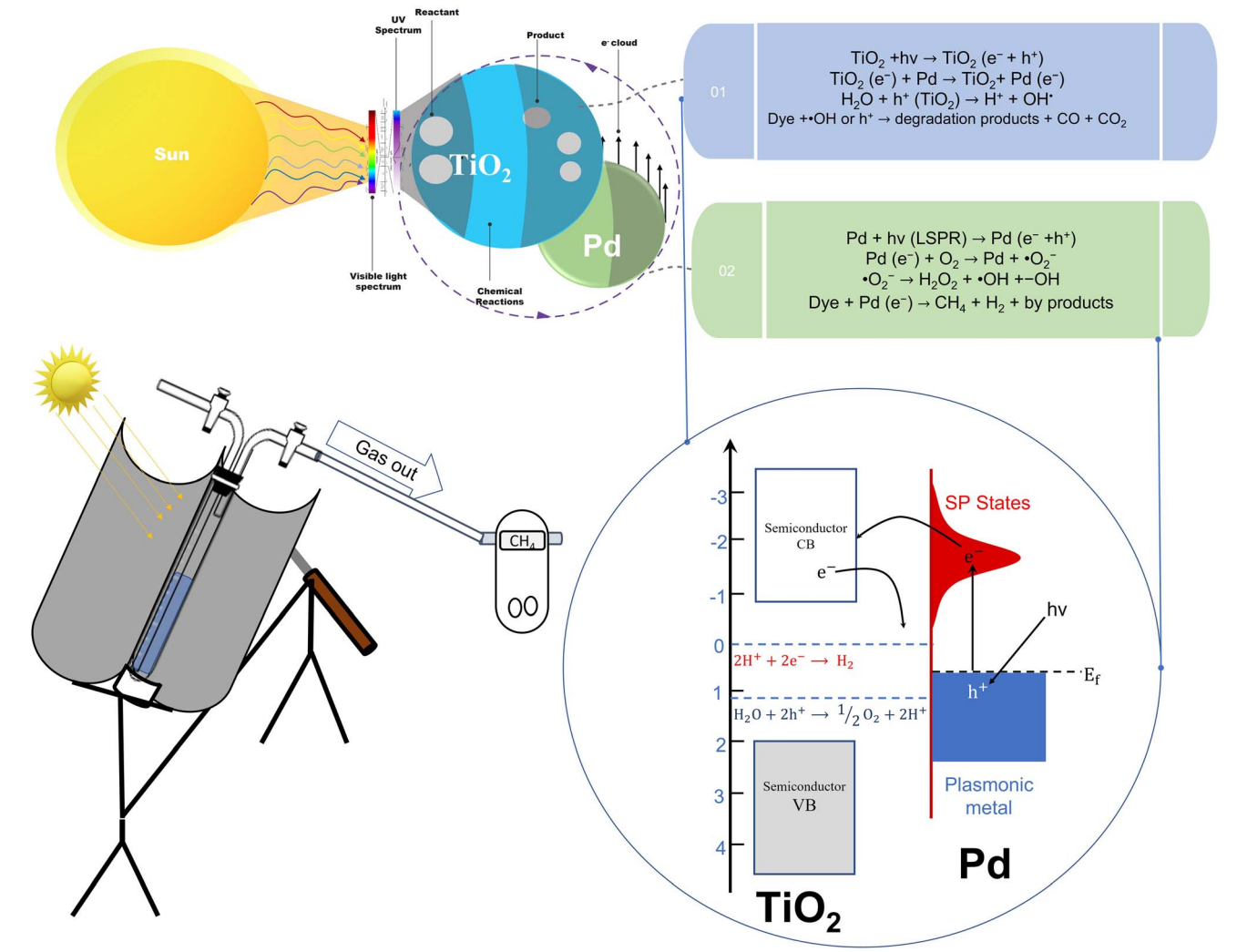

Fig. 10 A mechanistic schematic diagram of the occurred reactions in the photoreaction.

Under visible light, electron transfer from Pd's CB into its valence band results in the production of electron/hole charge carriers on the surface of the Pd-metal (eqn (9)). The interaction of conduction band electrons with oxygen molecules results in the creation of superoxide ($\cdot O^{2-}$) derivatives, as identified by eqn (10). Otherwise interaction with the dye molecules resulted in the reduction of the dye molecules into CH_4, H_2, and other by-products (eqn (11)).

Moreover, the same oxidizing behavior for superoxide $\cdot O_2$ may similarly go with H_2O interaction, forming the oxidizing species ($\cdot OH$) (eqn (12)).

$$Pd + h\nu\ (LSPR) \rightarrow Pd\ (e^- + h^+) \quad (9)$$

$$Pd\ (e^-) + O_2 \rightarrow Pd + \cdot O_2^- \quad (10)$$

$$\cdot O_2^- \rightarrow H_2O_2 + \cdot OH + {}^-OH \quad (11)$$

$$Dye + Pd\ (e^-) \rightarrow CH_4 + H_2 + \text{derivative by-products} \quad (12)$$

4 Conclusion

Dual functional Pd–TiO_2 plasmonic nanoparticles with different Pd-metal contents (3, 5, and 7% wt%) have been synthesized using a green-assisted fast microwave method using orange fruit peel extract as a capping agent. The XPS analysis proves the metallic form of palladium (Pd^0). The findings of optical properties and bandgap energy analysis revealed the increase in surface absorption as a consequence of plasmon excitation from noble metal nanoparticles incorporated into the TiO_2 matrix. The photocatalytic activity measurements confirm the higher efficiency of the prepared plasmonic photocatalysts than the commercially available TiO_2 Degussa P25. This has been attributed to the high specific surface area, the optical absorption in the visible region by the LSPR, and the excellent charge separation in the Pd–TiO_2 samples. In summary, the Pd–TiO_2 plasmonic photocatalysts are demonstrated to be promising dual functional materials in the photocatalytic eco-friendly transformation of organic dye pollutants and the generation of helpful fuel gases such as CH_4 and H_2 gases from the destruction of organic matter under sunlight illumination in an anaerobic environment.

Data availability

All data are fully available without restriction.

Author contributions

Mbrouk: data curation, methodology, resources, experimental work, and preliminary analysis supporting the original manuscript. Prof. Hafez and Prof. Saif invented and devised a work plan, collected data, and wrote the first manuscript of the article. Dr El-Shafey and Fawzy are both involved in the data analysis. Prof. Abdel-Mottaleb assisted with scientific oversight, text modification, and language enhancement. The final paper was critically evaluated and approved by all authors.

Conflicts of interest

There is no conflict of interest to declare.

Acknowledgements

This research work has been performed using facilities at Nanophochem. Lab, Environmental Studies and Research Institute, University of Sadat City. This work was supported financially by the Science and Technology Development Fund (STDF), Egypt, Grant No. TD-43380.

References

1 A. Thakur, P. Kumar, S. Bagchi, R. K. Sinha and P. Devi, *Sol. Energy*, 2019, **193**, 715–723.
2 O. Mbrouk, H. Hafez, S. Mozia, A. M. Othman and M. S. A. Abdel Mottaleb, *BMC Chem.*, 2022, **16**, 1–15.
3 M. Ramzan, S. A. Raza, M. Usman, G. D. Sharma and H. A. Iqbal, *J. Cleaner Prod.*, 2022, **333**, 130066.
4 A. Mills, R. Davies and D. Worsley., *Chem. Soc. Rev.*, 1993, 417–425.
5 X. Meng, L. Liu, S. Ouyang, H. Xu, D. Wang, N. Zhao and J. Ye, *Adv. Mater.*, 2016, **28**, 6781–6803.
6 W. Zhou, N. Umezawa, R. Ma, N. Sakai, Y. Ebina, K. Sano, M. Liu, Y. Ishida, T. Aida and T. Sasaki, *Chem. Mater.*, 2018, **30**, 6449–6457.
7 A. Kumar, P. Choudhary, A. Kumar, P. H. C. Camargo and V. Krishnan, *Small*, 2022, **18**, 2101638.
8 L. Qin, G. Wang and Y. Tan, *Sci. Rep.*, 2018, **8**(1), 1–13.
9 W. Li, X. s. Chu, F. Wang, Y. y. Dang, X. y. Liu, T. h. Ma, J. y. Li and C. y. Wang, *Appl. Catal., B*, 2022, **304**, 121000.
10 X. l. Hao, X. s. Chu, X. y. Liu and W. Li, *J. Colloid Interface Sci.*, 2022, **621**, 160–168.
11 P. Yilmaz, A. M. Lacerda, I. Larrosa and S. Dunn, *Electrochim. Acta*, 2017, **231**, 641–649.
12 M. de la Flor, R. Camarillo, F. Martínez, C. Jiménez, R. Quiles and J. Rincón, *J. Environ. Chem. Eng.*, 2021, **9**(5), 106278.
13 X. L. Hao, X. S. Chu, K. L. Luo and W. Li, *J. Catal.*, 2022, **411**, 226–234.
14 S. G. Ullattil and P. Periyat, *Sol. Energy*, 2017, **147**, 99–105.
15 B. M. Rajbongshi, A. Ramchiary, B. M. Jha and S. K. Samdarshi, *J. Mater. Sci.: Mater. Electron.*, 2014, **25**, 2969–2973.
16 M. S. Punnoose, D. Bijimol and B. Mathew, *Environ. Nanotechnol. Monit. Manag.*, 2021, **16**, 100525.
17 P. Periyat, B. Naufal and S. G. Ullattil, *Mater. Sci. Forum*, 2016, **855**, 78–93.
18 Ü. Özgür, Y. I. Alivov, C. Liu, A. Teke, M. Reshchikov, S. Doğan, V. Avrutin, S.-J. Cho and H. Morkoç, *J. Appl. Phys.*, 2005, **98**, 11.
19 T. U. D. Thi, T. T. Nguyen, Y. D. Thi, K. H. T. Thi, B. T. Phan and K. N. Pham, *RSC Adv.*, 2020, **10**, 23899–23907.

20 T. Teranishi and M. Miyake, *Chem. Mater.*, 1998, **10**, 594–600.
21 H. Hafez, M. Saif and M. S. A. Abdel-Mottaleb, *J. Power Sources*, 2011, **196**, 5792–5796.
22 E. M. Abdou, H. S. Hafez, E. Bakir and M. S. A. Abdel-Mottaleb, *Spectrochim. Acta, Part A*, 2013, **115**, 202–207.
23 O. A. Mbrouk, M. Fawzy, H. M. Elshafey, M. Saif, H. Hafez and M. S. A. Abdel Mottaleb, *Appl. Organomet. Chem.*, 2022, **36**, e6807.
24 J. Zhang and X. Bai, *Inorg. Nano-Met. Chem.*, 2017, **47**(5), 672–676.
25 K. H. Leong, H. Y. Chu, S. Ibrahim and P. Saravanan, *Beilstein J. Nanotechnol.*, 2015, **6**(43), 428–437.
26 M. Taghdiri and S. D. Doolabi, *Int. J. Photoenergy*, 2020, 8870194.
27 M. J. Sampaio, Z. Yu, J. C. Lopes, P. B. Tavares, C. G. Silva, L. Liu and J. L. Faria, *Sci. Rep.*, 2021, **11**(1), 1–11.
28 D. S. García-Zaleta, A. M. Torres-Huerta, M. A. Domínguez-Crespo, A. García-Murillo, R. Silva-Rodrigo and R. L. González, *J. Nanomater.*, 2016, 1805169.
29 M. G. Rinaudo, A. M. Beltrán, M. A. Fernández, L. E. Cadús and M. R. Morales, *Chemistry Proceedings*, 2020, **2**, 13.
30 F. Wang, X. Niu, W. Wang, W. Jing, Y. Huang and J. Zhang, *J. Taiwan Inst. Chem. Eng.*, 2018, **93**, 87–93.
31 Z. L. Wang, J. M. Yan, H. L. Wang, Y. Ping and Q. Jiang, *J. Mater. Chem. A*, 2013, **1**, 12721–12725.
32 J. B. Zhong, J. Z. Li, X. Y. He, J. Zeng, Y. Lu, W. Hu and K. Lin, *Curr. Appl. Phys.*, 2012, **12**, 998–1001.
33 K. Shoueir, S. Kandil, H. El-hosainy and M. El-Kemary, *J. Cleaner Prod.*, 2019, **230**, 383–393.
34 W. Li, X. Wang, Q. Ma, F. Wang, X. s. Chu, X. c. Wang and C. y. Wang, *Appl. Catal., B*, 2021, **284**, 119688.
35 R. Beranek, *Adv. Phys. Chem.*, 2011, **2011**, 786759.
36 X. Pan and Y. J. Xu, *Appl. Catal., A*, 2013, **459**, 34–40.
37 S. Y. Lee, I. H. Yoo, R. Singh, Y. J. Lee, S. S. Kalanur and H. Seo, *Appl. Surf. Sci.*, 2021, **570**, 151255.
38 D. Wang, S. C. Pillai, S. H. Ho, J. Zeng, Y. Li and D. D. Dionysiou, *Appl. Catal., B*, 2018, **237**, 721–741.
39 S. Lal, S. Link and N. J. Halas, *Nat. Photonics*, 2007, 641–648.
40 T. Chung, S. Y. Lee, E. Y. Song, H. Chun and B. Lee, *Sensors*, 2011, **11**, 10907–10929.
41 V. Kumari, S. Yadav, A. Mittal, K. Kumari, B. Mari and N. Kumar, *Inorg. Chem. Commun.*, 2020, **121**, 108241.
42 K. H. Leong, H. Y. Chu, S. Ibrahim and P. Saravanan, *Beilstein J. Nanotechnol.*, 2015, **6**(43), 428–437.